Bulletin of the Seismological Society of America, Vol. 95, No. 6, pp. 2066–2080, December 2005, doi: 10.1785/0120050081

Fréchet Kernels for Imaging Regional Earth Structure Based on Three-Dimensional Reference Models

by Li Zhao, Thomas H. Jordan, Kim B. Olsen, and Po Chen

Abstract High-resolution images of three-dimensional (3D) seismic structures are not only of scientific interest, but also of practical importance in predicting strong ground motion after large earthquakes. Given the source and station distributions, resolutions in current regional seismic tomography studies have been limited by two types of simplifying practices: the adoption of high-frequency approximations such as the ray theory and the use of one-dimensional (1D) reference (starting) models. We have developed a new approach to compute accurate finite-frequency 3D Fréchet (sensitivity) kernels of observed travel time and amplitude anomalies relative to 3D reference models. In our approach, we use a fourth-order staggered-grid finite-difference method to model the seismic-wave propagation in 3D media, and the reciprocity property of the Green's tensor to reduce the number of numerical simulations. This approach accounts for the perturbations in compressional- and shear-wave speeds in the same way, leading to a capability of inverting for the shear-wave speed directly from seismic data. The algorithm is readily parallelized to allow for realistic regional high-resolution 3D tomography inversions. We have implemented the algorithm for the Southern California Earthquake Center (SCEC) Community Velocity Model, SCEC CVM 3.0, a complex 3D model for Southern California including a number of sedimentary basins. By enabling the inversion of 3D structural perturbations to 3D reference models, our approach provides a practical means of iteratively solving the nonlinear regional tomography problems.

Introduction

Reliable prediction of strong ground motion following large earthquakes is essential in assessing earthquake hazards and taking precautionary measures in order to reduce the human and property losses from earthquakes. In recent years, with the advancement in high-performance computing, seismologists have developed computer codes using a variety of numerical algorithms such as finite-difference (e.g., Frankel and Vidale, 1992; McLaughlin and Day, 1994; Olsen, 1994; Graves, 1996; Aoi and Fujiwara, 1999; Kristek *et al.*, 1999), finite-element (e.g., Bao *et al.*, 1998; Aagaard *et al.*, 2001), pseudospectral (e.g., Tessmer *et al.*, 1992; Igel, 1999) and spectral-element (e.g., Komatitsch and Vilotte, 1998; Komatitsch *et al.*, 2004) methods to simulate the complete time history of the ground motion with the purpose of providing a numerical shake table for engineers.

The accuracy of the simulated strong ground motion depends heavily on a realistic regional earth model. The ground motion can be greatly influenced by the three-dimensional (3D) subsurface seismic structures, most notably in a sedimentary environment such as the Los Angeles Basin (Fig. 1), where the seismic ground motion is amplified not only by the relatively soft sedimentary material, but more importantly through the trapping of basin edge generated reflected and/or refracted waves inside the basin and the constructive interference of these waves (e.g., Kawase, 1996; Graves *et al.*, 1998; Pitarka *et al.*, 1998; Davis *et al.*, 2000; Olsen, 2000). In addition, mapping the small-scale structural variations in and around the basin is also important to studying the source properties of the numerous small local earthquakes.

Up to now, 3D studies of the structure in the L.A. Basin and vicinity have primarily been focused on the *P*-wave speed and coming from three sources: travel-time tomography (e.g., Kohler, 1997; Hauksson, 2000), linear-array active-source surveys (Fuis *et al.*, 2001; Godfrey *et al.*, 2002), borehole as well as sedimentary age-depth data (Magistrale *et al.*, 1996; Magistrale *et al.*, 2000), and industry-data analysis (Süss and Shaw, 2003). Thus, the currently available L.A. Basin regional models either do not have sufficient spatial resolution or do not cover the entire region. The Southern California Earthquake Center Community Velocity Model (SCEC CVM) is created by adopting the regional tomography result of Hauksson (2000) as the background model and using the borehole and sedimentary

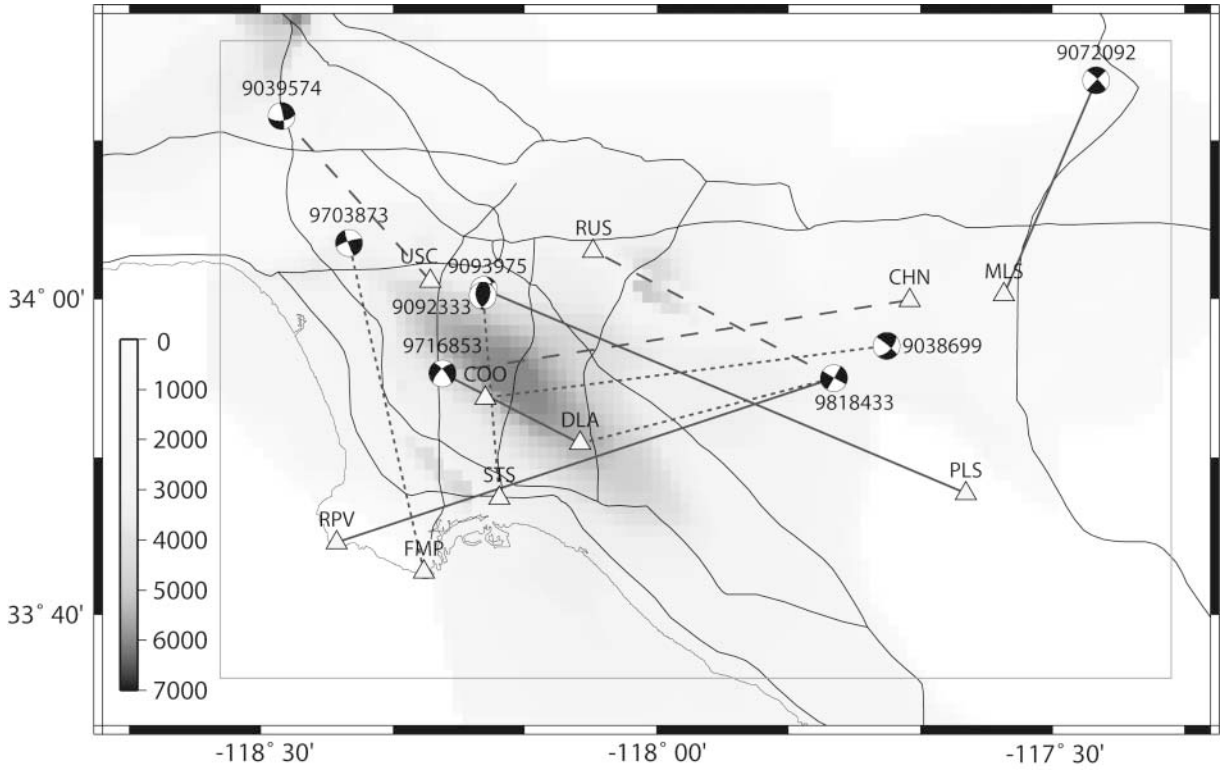

Figure 1. Map of the region around the Los Angeles Basin. The basin depths in meters are indicated by the grayscale. Beach balls show the locations and focal mechanisms of four earthquakes. Each earthquake has a seven-digit ID number assigned by the Southern California Earthquake Data Center where we obtained the recorded seismograms and the earthquake catalog. Triangles indicate the four California Integrated Seismic Network stations. The box shows the boundary of the region in which we conduct the calculations. The solid, dashed, and dotted lines are the paths for which numerical results are presented.

age-depth based structure for the basins (Magistrale *et al.*, 2000; Kohler *et al.*, 2003). Furthermore, the shear-speed models in all the studies cited above are not constrained by the data but are derived from the *P*-wave speeds through certain scaling relations between the two wave speeds. As a result, the current models are still insufficient for the prediction of regional high-resolution strong-motion maps that can lead to effective earthquake hazard analysis. Nevertheless, regional models such as the SCEC CVM do perform very well in predicting waveforms of the initial *P* wave up to a frequency of 1 Hz at most SCSN stations (P. Chen *et al.*, unpublished results, 2005) and even some of the shear-dominated waves at periods as short as 6 sec (Komatitsch *et al.*, 2004). The performance of the hybrid models is encouraging because they can serve as the reference models from which we can make phase and amplitude observations that can be used to refine the models through inversions. The purpose of this study is to develop an algorithm in order to accurately compute the Fréchet kernels that linearly relate the phase and amplitude measurements to perturbations of the seismic structure from the reference models. Such an algorithm will enable us to conduct seismic tomography in a fully 3D manner: inverting for 3D earth structure using accurate 3D Fréchet kernels computed in 3D reference models. This new fully 3D approach eliminates the high frequency and structural averaging approximations that are ubiquitous in current tomography studies and therefore provides a suitable tool of structural imaging for the USArray component of the EarthScope project.

Seismic Waveform Analysis

The waveforms recorded at seismic stations contain information on both the earthquake source that emits the seismic waves and the medium in which the waves propagate. By analyzing the waveforms, one can make quantitative measurements of this information and infer from it the source process and the medium property. The easiest and most common seismological measurements are the high-frequency (onset) arrival times of body waves and waveform amplitudes. These direct measurements, however, are not efficient in extracting source and structural information from the seismograms. High frequency or ray-theoretical approximation to body-wave arrival times requires smooth struc-

tural variations and is difficult to apply to 3D structures. On the other hand, since the seismic records originate from the complex interference among waves of different frequencies and from different paths, and phase and amplitude effects are entangled on the seismograms, instantaneous waveform amplitudes vary in a nonlinear fashion with model variations.

Gee and Jordan (1992) introduced the approach of generalized seismological data functional (GSDF) to making indirect waveform measurements. It involves a process in which the phase and amplitude variations in the waveforms are disentangled. The frequency-dependent phase and amplitude anomalies with respect to the reference source and structural models are then measured over a set of narrowband filters. This approach also provides a mechanism to account for the effects on the measurements due to the windowing and filtering operations in the measurement process and the interference effects from neighboring seismic phases. Measurements obtained through the GSDF approach have been used in regional structural inversions (e.g., Gaherty *et al.*, 1996; Katzman *et al.*, 1998), global finite-moment tensor inversions (McGuire *et al.*, 2001), and the structural and source investigations in the L.A. Basin (Chen *et al.*, 2005).

The GSDF approach is based on the cross correlation between the observed waveform $u(t)$ and its synthetic $\tilde{u}(t)$ for the initial or reference models of the source and structure. Cross correlation is a simple and accurate way of quantifying the phase and amplitude differences between two waveforms. For example, the travel-time anomaly $\delta\tau_p$ can be defined as the lag time at which the cross correlagram reaches the maximum. If the travel-time anomaly is small, it can be expressed as (Tanimoto, 1995; Zhao and Jordan, 1998; Dahlen *et al.*, 2000)

$$\delta\tau_{\mathrm{p}} = -\frac{\int_{t_1}^{t_2} \dot{\tilde{u}}(t)\delta u(t)dt}{\int_{t_1}^{t_2} |\dot{\tilde{u}}(t)|^2 \, dt}, \tag{1}$$

where $\delta u(t)$ is the waveform perturbation, namely, $\delta u(t) = u(t) - \tilde{u}(t)$, a dot represents the time derivative, and the integrals are over the time window $[t_1,t_2]$ enclosing the entire waveform of the arrival of interest. In this article, a wiggle always indicates a quantity in the reference model. The cross-correlation measurement $\delta\tau_{\mathrm{p}}$ reflects the integrated or averaged travel-time or phase shifts between the synthetic and recorded waveforms over the finite time window $[t_1,t_2]$. It is a generalization of the high-frequency (onset) arrival-time anomaly in the sense that the latter is merely a special case of the cross-correlation result in (1) at the limit of infinite frequency.

With the travel-time anomaly defined in equation (1), the amplitude anomaly can be measured by a parameter $\delta\tau_{\mathrm{q}}$ defined as

$$\exp(-\omega_{\mathrm{a}}\delta\tau_{\mathrm{q}}) = A/\tilde{A}, \tag{2}$$

where ω_{a} is the dominant angular frequency of the waveform, A is the amplitude of the cross correlagram at the lag time $\delta\tau_{\mathrm{p}}$, and $\tilde{A}$ is the maximum amplitude of the autocorrelagram of the synthetic seismogram. The amplitude anomaly has an expression similar to equation (1) for the travel-time anomaly:

$$\delta\tau_{\mathrm{q}} = -\frac{1}{\omega_{\mathrm{a}}}\frac{\int_{t_1}^{t_2} \tilde{u}(t)\delta u(t)dt}{\int_{t_1}^{t_2} |\tilde{u}(t)|^2 \, dt}, \tag{3}$$

Although the cross-correlation approach provides accurate phase and amplitude anomaly measurements $\delta\tau_{\mathrm{p}}$ and $\delta\tau_{\mathrm{q}}$, it does not fully explore the frequency-dependent nature of the seismic-wave propagation in the earth, for example, the well-known dispersion of surface waves. As demonstrated by Katzman *et al.* (1998), dispersion also widely occurs in body waves simply because a given body wave interacts with different parts of the earth model at different frequencies. Therefore, a given waveform has frequency-dependent phase and amplitude anomalies $\delta\tau_{\mathrm{p}}(\omega)$ and $\delta\tau_{\mathrm{q}}(\omega)$, and they also have frequency-dependent structural sensitivities (see plate 2 in Katzman *et al.*, 1998). We also note here that the quantities defined in equations (1) and (3) are delay-time and amplitude-reduction measurements: positive values for $\delta\tau_{\mathrm{p}}$ and $\delta\tau_{\mathrm{q}}$ represent delays in arrival time and decreases in amplitudes, respectively, of the records relative to the synthetics. Moreover, both types of measurements have the unit of time.

The GSDF approach is exactly designed to explore the frequency-dependent structural effects on seismic waves in order to extract more independent information from the waveforms to enhance the resolving power in the inversions. In this approach, phase and amplitude anomalies, denoted by $\delta\tau_{\mathrm{p}}(\omega_i)$ and $\delta\tau_{\mathrm{q}}(\omega_i)$, are measured from the cross correlagrams that have been time windowed and narrowband filtered around a set of frequencies ω_i. More importantly, the GSDF method provides the mathematical formula that express the waveform-derived measurements $\delta\tau_{\mathrm{p}}(\omega_i)$ or $\delta\tau_{\mathrm{q}}(\omega_i)$ as the averages of the heterogeneity-induced $\delta\tau_{\mathrm{p}}(\omega)$ and $\delta\tau_{\mathrm{q}}(\omega)$ over the corresponding time window and (narrow) frequency band. Details on the GSDF definition, measurement, and formulation can be found in Gee and Jordan (1992).

Fréchet Kernels for Seismic Delay Times and Amplitudes

Generally speaking, the source and structural effects are coupled in the GSDF measurements. As a result, a unified methodology can be designed so that both the source and structural variations can be inverted from the same GSDF

dataset in a mutually consistent manner. Inversion of the GSDF data for the finite-moment tensors of earthquakes is described in Chen *et al.* (2005). In this article, we discuss the structural component of this unified approach. In addition, we will focus on the delay-time and amplitude reduction $\delta\tau_p(\omega)$ and $\delta\tau_q(\omega)$ that are caused by the structural heterogeneities only. We first derive the expressions of their structural sensitivity functions or Fréchet kernels. Then we demonstrate some of the properties of these kernels using simple structural models. Finally, we present Fréchet kernels in realistic 3D reference models for data obtained from several local earthquakes.

According to the representation theorem (e.g., Aki and Richards, 2002), the perturbation of the displacement waveform can be expressed exactly as an integral over the volume of the earth model under study:

$$\delta\mathbf{u}(\mathbf{r}_R,t;\mathbf{r}_S) = -\int_{\oplus}\int_{-\infty}^{\infty}\tilde{\mathbf{G}}(\mathbf{r}_R,\tau;\mathbf{r})\cdot\left\{\delta\rho(\mathbf{r})\frac{\partial^2}{\partial\tau^2}\mathbf{I} - \nabla\cdot[\delta\mathbf{C}(\mathbf{r})\cdot\nabla]\right\}\cdot\mathbf{u}(\mathbf{r},t-\tau;\mathbf{r}_S)dt\,d^3\mathbf{r}, \quad (4)$$

where $\mathbf{r}_S$ and $\mathbf{r}_R$ are the locations of the source and receiver, respectively. The perturbations in density and the second-order elastic tensor are $\delta\rho$ and $\delta\mathbf{C}$, respectively. $\tilde{\mathbf{G}}(\mathbf{r}_R,\tau;\mathbf{r})$ is the Green's tensor from $\mathbf{r}$ to receiver $\mathbf{r}_R$ in the reference model, $\mathbf{u}(\mathbf{r},t-\tau;\mathbf{r}_S)$ is the displacement from earthquake source at $\mathbf{r}_S$ to $\mathbf{r}$ in the perturbed model, and $\mathbf{I}$ is the second-order identity tensor. Equation (4) is an exact yet nonlinear (implicit) equation since the displacement $\mathbf{u}(\mathbf{r},t-\tau;\mathbf{r}_S)$ is the wavefield in the perturbed model. Integrating by parts and applying the Gauss theorem, equation (4) can be rewritten in the form

$$\delta\mathbf{u}(\mathbf{r}_R,t;\mathbf{r}_S) = \int_{\oplus}\delta\mathbf{U}(\mathbf{r}_R,t;\mathbf{r};\mathbf{r}_S)\,d^3\mathbf{r}, \quad (5)$$

with the integration kernel

$$\delta\mathbf{U}(\mathbf{r}_R,t;\mathbf{r};\mathbf{r}_S) = -\int_{-\infty}^{\infty}\left[\delta\rho(\mathbf{r})\tilde{\mathbf{G}}\cdot\frac{\partial^2\mathbf{u}}{\partial\tau^2} + (\nabla\tilde{\mathbf{G}})^{213}:\delta\mathbf{C}(\mathbf{r}):(\nabla\mathbf{u})\right]dt, \quad (6)$$

where, for brevity, we have omitted the arguments for $\tilde{\mathbf{G}}(\mathbf{r}_R,\tau;\mathbf{r})$ and $\mathbf{u}(\mathbf{r},t-\tau;\mathbf{r}_S)$. The symbol $(\cdot)^{213}$ represents the transposition of the first and the second indices of a third-order tensor. In obtaining equation (6), we consider only the perturbations in density and elements of the elastic tensor. Perturbation of material discontinuities including the free surface requires perturbing the boundary conditions and is beyond the scope of this article. Substituting equations (5) and (6) into equations (1) and (3), we obtain the expressions for the delay time and amplitude reduction for the displacement waveform $\tilde{u}_l(\mathbf{r}_R,t;\mathbf{r}_S)$ polarized in direction $\hat{\mathbf{e}}_l$:

$$\delta\tau_p = \int_{\oplus}\delta T_p(\mathbf{r}_R;\mathbf{r};\mathbf{r}_S)\,d^3\mathbf{r}, \quad (7)$$

$$\delta\tau_q = \int_{\oplus}\delta T_q(\mathbf{r}_R;\mathbf{r};\mathbf{r}_S)\,d^3\mathbf{r}, \quad (8)$$

with the integration kernels:

$$\delta T_p(\mathbf{r}_R;\mathbf{r};\mathbf{r}_S) = \frac{1}{P_l}\int_{t_1}^{t_2}\tilde{u}_l(\mathbf{r}_R,t;\mathbf{r}_S)\left\{\hat{\mathbf{e}}_l\cdot\int_{-\infty}^{\infty}[\delta\rho(\mathbf{r})\tilde{\mathbf{G}}\cdot\frac{\partial^2\mathbf{u}}{\partial\tau^2} + (\nabla\tilde{\mathbf{G}}):\delta\mathbf{C}(\mathbf{r}):(\nabla\mathbf{u})]\right\}d\tau\,dt, \quad (9)$$

$$\delta T_q(\mathbf{r}_R;\mathbf{r};\mathbf{r}_S) = \frac{1}{Q_l}\int_{t_1}^{t_2}\tilde{u}_l(\mathbf{r}_R,t;\mathbf{r}_S)\left\{\hat{\mathbf{e}}_l\cdot\int_{-\infty}^{\infty}[\delta\rho(\mathbf{r})\tilde{\mathbf{G}}\cdot\frac{\partial^2\mathbf{u}}{\partial\tau^2} + (\nabla\tilde{\mathbf{G}}):\delta\mathbf{C}(\mathbf{r}):(\nabla\mathbf{u})]\right\}d\tau\,dt, \quad (10)$$

where the normalization factors are

$$P_l = \int_{t_1}^{t_2}|\ddot{\tilde{u}}_l(t)|^2\,dt, \quad \text{and} \quad Q_l = \omega_a\int_{t_1}^{t_2}|\tilde{u}_l(t)|^2\,dt. \quad (11)$$

Thus the inversions of the delay times and amplitude reductions for a specific model parameter m are enabled by the Fréchet or sensitivity kernels defined in the following way:

$$\delta\tau_p = \int_{\oplus}K_p^m(\mathbf{r})\delta m(\mathbf{r})d^3\mathbf{r}. \quad (12)$$

$$\delta\tau_q = \int_{\oplus}K_q^m(\mathbf{r})\delta m(\mathbf{r})d^3\mathbf{r}. \quad (13)$$

By the definitions in equations (12) and (13), the Fréchet kernels $K_p^m(\mathbf{r})$ and $K_q^m(\mathbf{r})$ linearly relate the delay times and the amplitude reductions, respectively, to the perturbations of model parameters. Explicit expressions for the Fréchet kernels of a specific model parameter m can be derived from equations (7)–(10) by taking the limit

$$K_p^m(\mathbf{r}) = \lim_{\delta\bar{m}\to 0}\left[\frac{\delta\tau_p}{\delta m(\mathbf{r})}\right], \quad \text{and} \quad K_q^m(\mathbf{r}) = \lim_{\delta\bar{m}\to 0}\left[\frac{\delta\tau_q}{\delta m(\mathbf{r})}\right], \quad (14)$$

where $\delta\bar{m}$ is a proper global measure of the perturbation of

the model parameter m from the reference model, for example, the maximum absolute value of $\delta m(\mathbf{r})$. By virtue of the fact that

$$\lim_{\delta \bar{m} \to 0} \mathbf{u} = \tilde{\mathbf{u}}, \tag{15}$$

we can simply replace the perturbed field $\mathbf{u}$ in equations (9) and (10) by its counterpart in the reference model $\tilde{\mathbf{u}}$, thus linearizing the problem. For the perturbations in the isotropic P- and S-wave speeds, the expressions for the delay-time and amplitude-reduction Fréchet kernels are

$$K_{\mathrm{p}}^{\alpha}(\mathbf{r}) = -\frac{1}{P_{\mathrm{I}}} \int_{t_1}^{t_2} 2\tilde{\rho}\tilde{\alpha}\dot{\tilde{u}}_{\mathrm{I}}(\mathbf{r}_{\mathrm{R}}, t; \mathbf{r}_{\mathrm{S}}) \int_{-\infty}^{\infty} \tilde{\mathbf{e}}_{\mathrm{I}} \cdot [(\nabla \cdot \tilde{\mathbf{G}}^{\mathrm{T}})(\nabla \cdot \tilde{\mathbf{u}})] d\tau \, dt, \tag{16}$$

$$K_{\mathrm{q}}^{\alpha}(\mathbf{r}) = -\frac{1}{Q_{\mathrm{I}}} \int_{t_1}^{t_2} 2\tilde{\rho}\tilde{\alpha}\tilde{u}_{\mathrm{I}}(\mathbf{r}_{\mathrm{R}}, t; \mathbf{r}_{\mathrm{S}}) \int_{-\infty}^{\infty} \tilde{\mathbf{e}}_{\mathrm{I}} \cdot [(\nabla \cdot \tilde{\mathbf{G}}^{\mathrm{T}})(\nabla \cdot \tilde{\mathbf{u}})] d\tau \, dt, \tag{17}$$

$$K_{\mathrm{p}}^{\beta}(\mathbf{r}) = \frac{1}{P_{\mathrm{I}}} \int_{t_1}^{t_2} 2\tilde{\rho}\tilde{\beta}\dot{\tilde{u}}_{\mathrm{I}}(\mathbf{r}_{\mathrm{R}}, t; \mathbf{r}_{\mathrm{S}}) \int_{-\infty}^{\infty} \tilde{\mathbf{e}}_{\mathrm{I}} \cdot \{(\nabla\tilde{\mathbf{G}})^{213} : [(\nabla\tilde{\mathbf{u}}) + (\nabla\tilde{\mathbf{u}})^{\mathrm{T}}] - 2(\nabla \cdot \tilde{\mathbf{G}}^{\mathrm{T}})(\nabla \cdot \tilde{\mathbf{u}})\} d\tau \, dt, \tag{18}$$

$$K_{\mathrm{q}}^{\beta}(\mathbf{r}) = \frac{1}{Q_{\mathrm{I}}} \int_{t_1}^{t_2} 2\tilde{\rho}\tilde{\beta}\dot{\tilde{u}}_{\mathrm{I}}(\mathbf{r}_{\mathrm{R}}, t; \mathbf{r}_{\mathrm{S}}) \int_{-\infty}^{\infty} \tilde{\mathbf{e}}_{\mathrm{I}} \cdot \{(\nabla\tilde{\mathbf{G}})^{213} : [(\nabla\tilde{\mathbf{u}}) + (\nabla\tilde{\mathbf{u}})^{\mathrm{T}}] - 2(\nabla \cdot \tilde{\mathbf{G}}^{\mathrm{T}})(\nabla \cdot \tilde{\mathbf{u}})\} d\tau \, dt, \tag{19}$$

where the superscript T represents the transpose of a second-order tensor. Note that in these expressions for the kernels at a location $\mathbf{r}$, $\tilde{\mathbf{G}}$ is the Green's tensor from $\mathbf{r}$ to the station at $\mathbf{r}_{\mathrm{R}}$ and $\tilde{\mathbf{u}}$ is the displacement field at $\mathbf{r}$ due to the earthquake at $\mathbf{r}_{\mathrm{S}}$, and both wavefields are evaluated in the reference model.

Equations (12), (13), and (16)–(19) provide the theoretical framework of the seismic structural inverse problem. The difficulty and resolution of a specific tomography approach depend on the level of complexity of three major elements in the inverse problem. They are the model perturbation $\delta m(\mathbf{r})$, the Fréchet kernel $K(\mathbf{r})$, and the reference model $\tilde{m}(\mathbf{r})$ in which the Green's tensor $\tilde{\mathbf{G}}$ and the wavefield $\tilde{\mathbf{u}}$ are calculated. All three elements are intrinsically three-dimensional functions. However, in almost all tomography inversions conducted so far, the Fréchet kernels and/or the reference models are assumed to be 1D or 2D based on research interests and due to the computational limitations. The choice of the reference model dictates the wave-propagation theory needed to compute the Green's tensor $\tilde{\mathbf{G}}$ and the wavefield $\tilde{\mathbf{u}}$. For instance, ray theory is appropriate as long as the reference structure varies smoothly for the seismic waves and therefore it is usually identified as a high-frequency approximation, whereas normal-mode theory can be used as an exact approach in a radially symmetric reference model. On the other hand, reducing the dimensionality of the Fréchet kernel implies structural averaging (smoothness) of the model perturbation $\delta m(\mathbf{r})$. For example, Fermat approximation (no ray-path change due to model perturbation) produces kernels that are nonzero only on the geometrical ray paths by averaging the structure in the plane perpendicular to the ray path, path-average assumption leads to only depth-dependent kernels after averaging in both horizontal dimensions, and cross-path stationary-phase approximation reduces the kernels to 2D functions within the source-station great-circle plane with the averaging in the transverse direction. Numerical modeling (Baig and Dahlen, 2003) shows that the structural averaging is valid only when the model perturbation is smooth over the first Fresnel zones of the seismic waves.

The problem with using ray theory and Fermat kernels in seismic tomography is obvious in imaging global shear-wave structure where intermediate-to long-period records (50 sec and longer) are used. Li and Tanimoto (1993) proposed a remedy in which the ray theory and Fermat approximations are replaced by the normal-mode theory and a cross-path stationary-phase approximation, respectively. The Fréchet kernels were no longer concentrated on the ray path but were 2D functions distributed in a 2D zone around the ray paths in the source-receiver great circle planes. This approach has been applied to both global (Li and Romanowicz, 1996; Mégnin and Romanowicz, 2000) and regional (Katzman *et al.*, 1998) studies. More recently, algorithms for computing 3D Fréchet kernels have been developed for global and regional tomography inversions, including the ray-theoretical approach for smooth 1D reference models that enables efficient calculations for geometrical arrivals (Dahlen *et al.*, 2000; Hung *et al.*, 2000) and the normal-mode approach for arbitrary arrivals in general 1D reference models (Zhao *et al.*, 2000).

So far, tomography studies for crustal structure on regional to local scales have primarily been the inversions of the P-wave travel times based on the Fermat approximation and ray theory, namely, the travel-time anomaly at a station is regarded as accumulated along the geometrical ray path between the earthquake and the station, and the structure away from the ray path has no effect on travel time. As discussed before, this approximation requires a smooth structural variation in both the reference model and the perturbed model. Therefore, it not only limits the resolving power of the tomography inversions but may also be invalid when complex 3D models must be used as reference models. P. Chen *et al.* (unpublished results, 2005) demonstrates that for seismic records at the Southern California Seismic Network stations from local earthquakes, simple 1D models are insufficient and 3D models such as the SCEC CVM 3.0 model must be used. Based on these considerations, we adopt the finite-difference methods as our wave-propagation theory

and compute the 3D Fréchet kernels for the delay times and amplitude reductions. This approach permits us to conduct nonlinear tomography inversions by iteratively updating the reference models, obtaining new measurements and Fréchet kernels, and inverting again for new models. Tromp *et al.* (2005) presented a different implementation in which the spectral-element method was used in computing the Fréchet kernels of the GSDFs based on an adjoint formulation.

In the next section, we discuss issues related to the implementation of expressions for computing the Fréchet kernels. Numerical results are presented in the sections "Fréchet Kernels in a Uniform Half-Space" and "Fréchet Kernel for Records from Local Earthquakes."

Implementation of the Expressions for the 3D Fréchet Kernels

From equations (16)–(19) we can see that in order to compute the value of a Fréchet kernel at a specific location $\mathbf{r}$, we need to have $\tilde{\mathbf{u}}(\mathbf{r}, t; \mathbf{r}_S)$, the displacement field from the earthquake source at $\mathbf{r}_S$ to $\mathbf{r}$ and $\tilde{\mathbf{G}}(\mathbf{r}_R, t; \mathbf{r})$, the Green's tensor from $\mathbf{r}$ to the receiver at $\mathbf{r}_R$; the spatial derivatives of these field variables at $\mathbf{r}$; and $\tilde{\mathbf{u}}(\mathbf{r}_R, t; \mathbf{r}_S)$, the displacement field from the source directly to the receiver. In computing the displacement and the Green's tensor, we adopt the staggered-grid finite-difference algorithm (Olsen, 1994) with precisions of fourth order in space and second order in time. This finite-difference algorithm includes an accurate treatment of the free-surface boundary condition (Gottschaemmer and Olsen, 2001) and adopts the method of perfectly matched layers (PML) formulated for fourth-order staggered grids for the absorbing boundary condition (Marcinkovich and Olsen, 2003). The kernels are evaluated at the same grid points that are used for the finite-difference calculations. Since each finite-difference simulation provides the three-component wave fields from a given source at all the grid points, the displacements $\tilde{\mathbf{u}}(\mathbf{r}, t; \mathbf{r}_S)$ and $\tilde{\mathbf{u}}(\mathbf{r}_R, t; \mathbf{r}_S)$ are obtained in the same finite-difference simulation. However, the calculation of the Green's tensor $\tilde{\mathbf{G}}(\mathbf{r}_R, t; \mathbf{r})$ would be prohibitively heavy if we had to run the finite-difference simulations from each grid point $\mathbf{r}$. A well-known approach to reduce the number of numerical simulations in computing the Green's tensors from all the grid points to a receiver is to apply the principle of reciprocity for the Green's tensors (e.g., Aki and Richards 2002) between $\mathbf{r}$ and receiver $\mathbf{r}_R$:

$$\tilde{\mathbf{G}}(\mathbf{r}_R, t; \mathbf{r}) = \tilde{\mathbf{G}}^T(\mathbf{r}, t; \mathbf{r}_R). \tag{20}$$

As a result, the Green's tensors from all the grid points to the receiver at $\mathbf{r}_R$ can be obtained by only three finite-difference simulations, for the unit impulsive point forces in three basis directions, using $\mathbf{r}_R$ as the source. With the reciprocity consideration, for each source-station pair, only four finite-difference simulations are needed to compute the Fréchet kernels for all the delay-time and amplitude-reduction measurements that can be obtained from the three-component seismic record. After the finite-difference calculations, we obtain the divergence and gradients of the wave fields by numerical differentiations. They are subsequently transformed to the frequency domain to compute the convolutions appearing in equations (16)–(19) as the integrals over τ. The results are then transformed back to the time domain to evaluate the time integrals over the window $[t_1, t_2]$. This algorithm can be implemented on both shared-memory and distributed-memory systems. To compute all the kernels for a three-component record at a station with 4000 timesteps and 2.5 million spatial grid points, it takes ~10 hours on a shared-memory SUN Server with eight 750 MHz processors, and 80% of the CPU time is spent on the four finite-difference simulations. In tomography practices, the number of finite-difference simulations can be further reduced. Since the Green's tensors $\tilde{\mathbf{G}}(\mathbf{r}_R, t; \mathbf{r})$ are for specific stations and do not depend on actual earthquakes, they can be computed for all the stations and kept in storage. Then for each earthquake only one finite-difference simulation is necessary.

Fréchet Kernels in a Uniform Half-Space

As a first numerical experiment of the algorithm, we choose the simplest reference model: a half-space having constant density and *P*- and *S*-wave speeds and a free surface. Both the source and the receiver are buried at a depth of 24 km to reduce the effect of the free surface on the direct arrivals, and the source-receiver distance is 32.2 km. The Cartesian coordinate system is chosen such that the *x*-axis points from the receiver to the source and the *z*-axis points upward. The model parameters are $\rho = 3000\text{kg/m}^3$ $\alpha = 6500\text{m/sec}$ and $\beta = 3500$ m/sec. The source-time function commonly used in finite-difference modeling has a Gaussian form

$$s(t) = \exp[-a(t - b/2)^2], \tag{21}$$

where the parameter a controls the characteristic width of the source-time function and ultimately the maximum frequency of the synthetic seismogram, and b specifies the time it takes for the source-time function to reach the maximum. Here we choose $a = 60$ and $b = 0.65$, resulting in synthetics with maximum frequency of about 2 Hz. We consider two types of sources: an explosive (isotropic) source and a double-couple one.

Explosive Source

Buried in a uniform medium under the free surface, the explosive source emits only a *P* wave, and there can be only three arrivals at the buried receiver: the direct *P* wave and the free surface reflected *pP* and *pS* waves.

The Fréchet kernels for *P*-wave speed α for the direct *P*-wave travel-time and amplitude anomalies measured on

the X-component seismogram are shown in Figure 2. In the uniform half-space model, the *P*-wave ray path is the straight line between the source S and the receiver R. Also plotted is the X-component waveform computed by the finite-difference method. In this and the rest of the waveform plots in this section, the portions of the waveform in red indicate the time window $[t_1, t_2]$ over which the delay times and amplitude reductions are measured and the corresponding kernels are computed. From the patterns of the Fréchet kernels in Figure 2, we can see immediately that even at the relatively short period of 0.5 sec that dominate the seismic waveform, the sensitivities of the *P*-wave delay time and amplitude reduction are not concentrated on the ray path, but extend as far as about 8 km away from it. We also see the counterintuitive phenomenon of the vanishing delay-time sensitivity on the ray path. This so-called banana-doughnut shape of the delay-time kernel has been observed and explained in a number of previous studies (Marquering *et al.*, 1999; Dahlen *et al.*, 2000; Hung *et al.*, 2000; Zhao *et al.*, 2000). It is the typical behavior of single-path, minimum-time geometrical body waves. However, this behavior apparently does not hold near the source and the receiver because of the complex and nongeometrical near-field contributions. A recent study suggests that the near-field region in which geometrical ray theory is invalid extends to at least twice the wavelength from the station (Favier *et al.*, 2004). In the first Fresnel zone roughly delineated by an ellipsoidal surface at the first sign change in the amplitude of the kernels, the delay-time sensitivity is mostly negative (warm color), indicating a natural behavior that a *P*-wave speed increase results in an advance in *P*-wave arrival time. On the other hand, the amplitude sensitivity is mostly positive, suggesting that a *P*-wave speed increase leads to a positive $\delta\tau_q$ or an amplitude reduction (see equation 2). This result can be qualitatively explained by the diffraction of the *P*-wave energy away from its geometrical ray path when the wave speed there is increased. This defocusing effect leads to a reduction in the *P*-wave amplitude at the receiver.

Figures 3 and 4 show the delay-time and amplitude-reduction Fréchet kernels for α for the X-component *pP* and *pS* waves, respectively. We can observe properties similar to those seen in Figure 2 in the kernels for the direct *P* wave, such as the banana-doughnut distribution in the delay-time kernels as well as the negative and positive amplitudes in the first Fresnel zone in the delay-time and amplitude-reduction kernels. However, the sensitivities for these surface-reflected waves extend to a more distant region from the ray paths than the direct *P* wave due to longer ray paths, demonstrating the effect of the propagation distance on the width of the first Fresnel zone. Also can be seen in Figure 3 are the spatially much more rapidly oscillating oval-ring shaped (egg shells in 3D) distributions. They result from the scatterings of the direct *P* wave *P* wave (larger set of rings) and to *S* wave (smaller set of rings). These *P*-to-*P* and *P*-to-*S* scattered waves arrive within the time window in which the *pP* measurements are made.

Even though the overall patterns in the Fréchet kernels can be explained very well by the physics of wave propagation, there are still persistent and spatially highly oscillatory patterns that are the results of numerical noises, as can be seen in the wispy tail near the source S in Figure 2. These numerical noises can be caused by the numerical dispersion

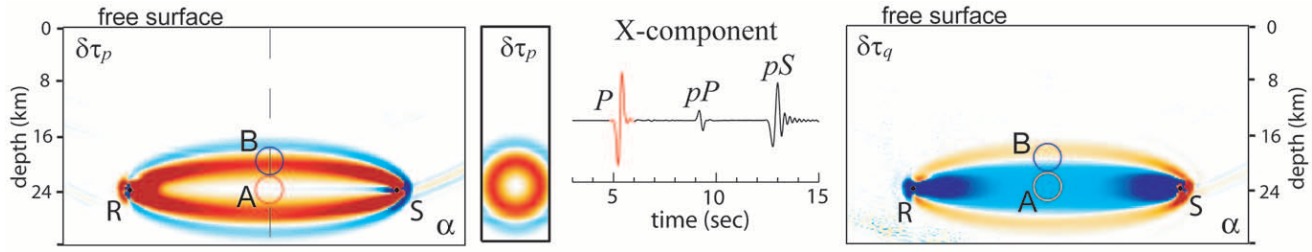

Figure 2. Numerical results for the *P* wave from an explosive source in a uniform half-space. Plotted are the X-component finite-difference synthetic and the Fréchet kernels of the X-component delay time $\delta\tau_p$ and amplitude reduction $\delta\tau_q$ for the *P*-wave speed α. The source and receiver, denoted by S and R, respectively, have a distance of 32.2 km and are both at the same depth of 24 km. X is the direction from receiver to the source, and Z is upward. The banana-doughnut phenomenon can be seen in the two plots for the delay time kernel in the source-receiver vertical plane and the transverse plane midway (dashed line) between the source and the receiver. The red and blue circles around points A and B indicate the locations of the model perturbation used in the numerical test discussed later. In this and subsequent waveform plots in this section, the waveform in the time window $[t_1, t_2]$ over which $\delta\tau_p$ and $\delta\tau_q$ are measured is always highlighted in red. In all the plots for the kernels, the color schemes are such that white represents zero; warm colors (yellow to orange to red) represent negative amplitudes indicating that a velocity increase leads to an advance in arrival time and an increase in amplitude; and cool colors (light to dark blue) represent positive amplitudes indicating a velocity increase leads to a delay in arrival time and a reduction in amplitude.

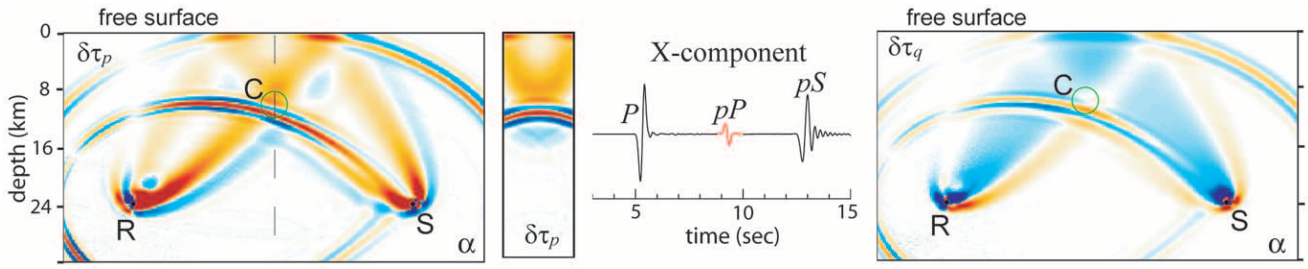

Figure 3. Same as Figure 2 but for the *pP* wave for the same synthetic as in Figure 2. Plotted are the Fréchet kernels of the delay time $\delta\tau_p$ and amplitude reduction $\delta\tau_q$ for the *P*-wave speed α. The $\delta\tau_p$ kernel is plotted in the source-receiver vertical plane and the transverse plane midway between the source and the receiver indicated by the dashed line. The green circle around point C indicates the location of the model perturbation used in the numerical test discussed later.

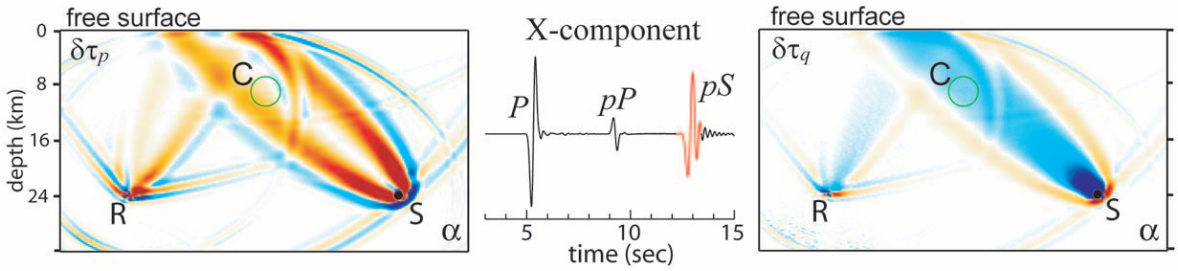

Figure 4. Same as Figure 2 but for the *pS* wave for the same synthetic as in Figure 2. Plotted are the Fréchet kernels of the delay time $\delta\tau_p$ and amplitude reduction $\delta\tau_q$ for the *P*-wave speed α.

in the finite-difference method, the inaccuracies in the free surface and absorption boundary conditions, and the forward and inverse fast Fourier transformations in our frequency-domain implementation of the convolutions in equations. (16)–(19). Because of rapid spatial oscillations, the integrals of these numerical noises are always negligible. Regardless, care must be taken in setting up the simulation parameters such as the dimensions of the simulation volume, the grid spacing, timestep, and the parameters a and b in equation (21) for the source-time functions.

In order to validate that the Fréchet kernels can correctly predict the arrival-time and amplitude perturbations, we conduct a numerical experiment in which we perturb the starting model by increasing both the *P*- and *S*-wave speeds in a sphere centered at three different points shown by the red and blue circles in Figure 2 and the green circle in Figures 3 and 4: point A midway on the direct-wave ray path; point B, which is 6 km above point A; and point C located at a depth of 10 km beneath the *pP* surface bounce point. Each of the wave-speed perturbations is such that it is at a maximum of 5% (in $\delta\alpha/\alpha$ or $\delta\beta/\beta$) at the center of the sphere and decreases with the distance from the center in a cosine square fashion until it reaches zero at a distance of 3 km. The waveforms for these three perturbed models are compared with that for the original uniform half-space in Figure 5. It can be seen that in the synthetic seismogram for the perturbation around point A (red line), the *P*-wave amplitude is reduced due to the defocusing effect, as predicted by the $\delta\tau_q$ kernel in Figure 2. However, the entire *P* waveform is widened such that the travel time as measured by the cross correlation of the entire *P* waveforms remains unchanged. On the other hand, for a perturbation around point B, the *P* wave is advanced (blue line) whereas its amplitude remains the same. This is also consistent with the predictions of the kernels in Figure 2. For a perturbation around point C, the *pP* wave is advanced (green line) and its amplitude is increased. The *pS* wave is slightly advanced while its amplitude is decreased. Therefore, all the waveform comparisons are consistent with the Fréchet kernel predictions.

Double-Couple Source

We next consider the situation of a double-couple source in the uniform half-space. The focal plane has a strike in the direction of the *y*-axis and a dip of 45° and the rake is also 45°. A double-couple source buried in a uniform half-space emits both *P* and *S* waves. Thus there are six arrivals at the receiver: the direct *P* and *S* waves and the free surface reflected *pP*, *pS*, *sP*, and *sS* waves. For the uniform half-space model used here and the source-receiver geometry shown in Figure 6, these phases arrive in three time windows. The first is the direct *P* wave at around 5 sec. Then the direct *S* wave and the surface reflected *pP* wave arrive

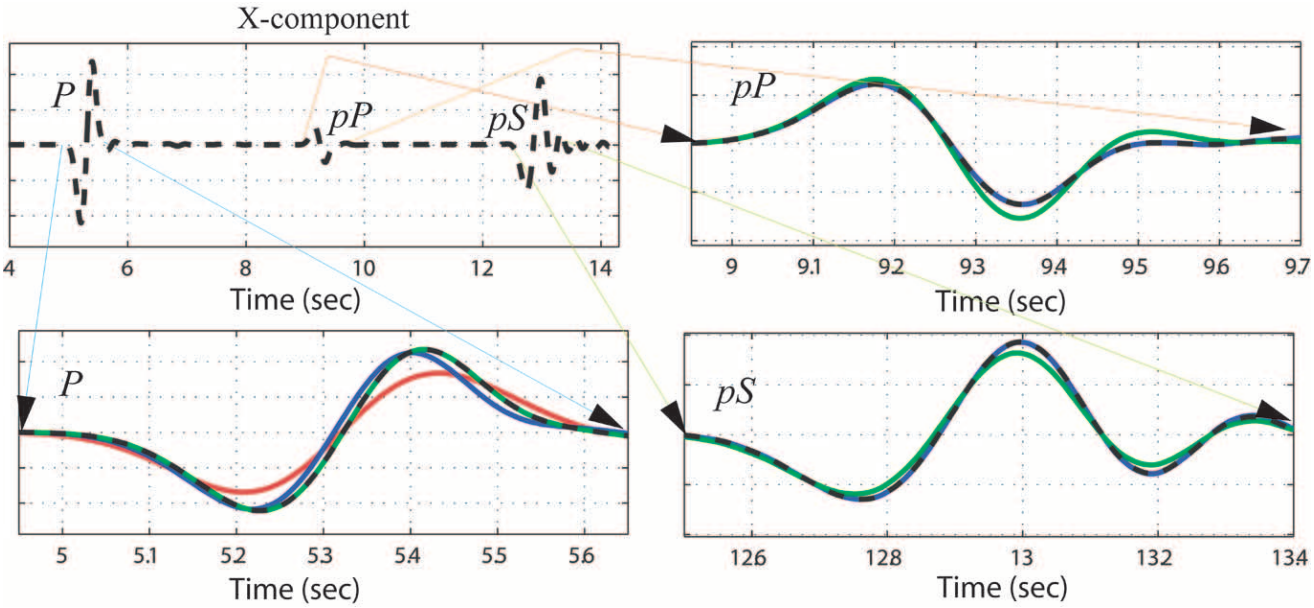

Figure 5. Comparisons of the X-component seismograms for the original uniform half-space model and three perturbed models. The locations of the three perturbations are shown in Figures 2, 3, and 4 by the red, blue, and green circles around points A, B, and C, respectively. The black dashed lines are the waveform for the original model and the perturbed waveforms are plotted by the same colors as those for the circles for the perturbation locations. The model perturbations and the resulting waveform changes are described in the text. The upper left plot shows the entire reference time series. The other three plots are blow-ups around the three specific seismic phases.

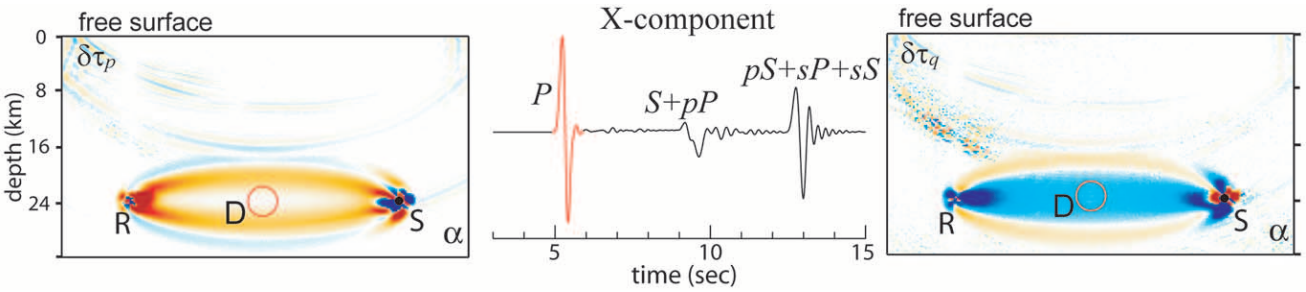

Figure 6. Numerical results for the X-component of the *P* wave from a double-couple source in a uniform half-space. The kernels for the *P*-wave speed α are plotted. The focal mechanism has a strike in Y direction, a dip of 45°, and a rake of 45°. The red circle around points D indicates the location of the model perturbation used in the numerical test discussed later.

at around 9 sec. Finally *pS, sP*, and *sS* arrive almost together right after 12 sec.

The Fréchet kernels for the direct *P* wave in Figure 6 show similar patterns as those for the *P* wave from an explosive source. However, near the source the pattern is more complicated. The reason for this is that for a double-couple source, the *P*-wave Fréchet kernel changes sign with direction according to the *P*-wave radiation amplitude that varies with takeoff angle and the azimuth. As a result, the kernels near the source have a four-lobe pattern. This is further complicated by near-field *P*-and-*S* coupling and the sign change from one Fresnel zone to another, thus resulting in an even more complicated pattern near the source. Farther away from the source, the kernels have significant amplitude only in the first Fresnel zone in which all the waves come from the source within a rather small solid-angle range with no sign change in the *P*-wave radiation amplitude. The kernels for the direct *S* wave on the Y-component are shown in Figure 7. The patterns are largely the same as those for the direct *P* wave, only the widths are smaller due to the smaller wavelength of the *S* wave. The delay-time kernel for the third group of arrivals $pS+sP+sS$ is shown in Figure 8. The pattern is more complicated than the delay-time kernel in Figure 4 because of the competing contributions of the dif-

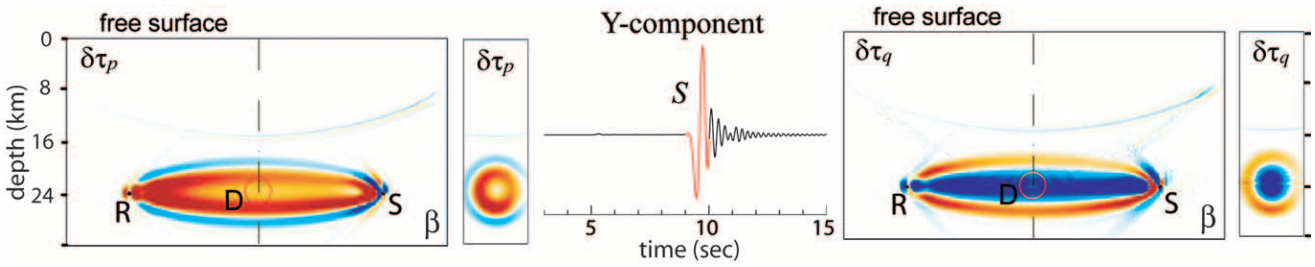

Figure 7. Numerical results for the Y-component of the *S* wave from the same double-couple source as in Figure 6 in a uniform half-space. The kernels for the *S*-wave speed β are plotted. The red circle around point D indicates the location of the model perturbation used in the numerical test discussed later.

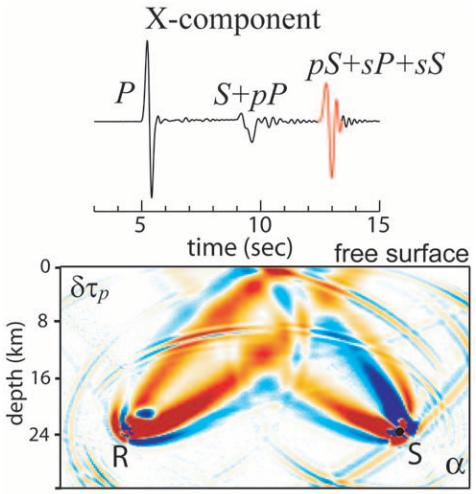

Figure 8. Numerical results for the X-component of the $pS+sP+sS$ wavegroup from the same double-couple source as in Figure 6 in a uniform half-space. Plotted is the kernel for the *P*-wave speed α.

ferent Fresnel zones of the *pS, sP*, and *sS* waves. Still, the kernel is dominated by the two *P*-wave legs in the *pS* and *sP* phases.

Shown in Figure 9 is the result of an experiment for the double-couple source in which we perturb the model in a sphere around point D (Figs. 6, 7). The shape, amplitude, and extent of the perturbation are the same as those in the numerical experiments for the explosive source. The resulting *P* wave has no travel-time change (red line) but a reduction in amplitude, whereas the *S* wave is slightly advanced and its amplitude is significantly reduced. Once again the waveform comparisons are consistent with the predictions of the kernels in Figures 6 and 7.

Fréchet Kernels for Records from Local Earthquakes

In this section we present numerical results for the Fréchet kernels in realistic 3D reference models. We use events and stations in and around the Los Angeles Basin. Locations of the events and stations are indicated in Figure 1. The reference model is the SCEC CVM 3.0 model (Kohler *et al.*, 2003; Magistrale *et al.*, 2000) for southern California. This regional 3D model combines information from multiple sources. In particular, for the L.A. Basin and a number of other sedimentary basins in the region, the *P*-wave speed is determined by empirical relationships from the sediment's depth and age, and the *S*-wave speed is obtained by scaling the *P*-wave speed with a constant Poission's ratio. Furthermore, in the top 300 m, the *P*- and *S*-wave speeds are constrained independently by borehole data. The densities in the basin models are also derived from the *P*-wave model. Outside the basins, a tomography model (Hauksson *et al.*, 2000) for the 3D wave-speed structure and a Moho depth model obtained from receiver function analysis (Zhu and Kanamori, 2000) are adopted. The 3D basin model presents quite a challenge to numerical simulations because the *S*-wave speed near the surface drops to as low as ~100 m/sec. In order for the numerical computations to be manageable, we slightly modify the SCEC CVM 3.0 model by clamping the density and *P*- and *S*-wave speeds at 2 g/cm^3, 2.5 km/sec, and 1.5 km/sec, respectively. In all the numerical examples discussed in this section, the dominant period in the calculations is about 1.5 sec.

The Fréchet kernels in Figure 10 are for the direct *P* waves along four paths (solid lines in Fig. 1). They reflect the sensitivities of the direct *P* waves to the *P*-wave speed α. Also plotted are the recorded seismograms and the corresponding synthetics in the SCEC CVM 3.0 model. The first observation from these images of the kernels is that at such a short period, the sensitivities of these body waves are not concentrated on the geometrical ray paths but spread around the ray paths over a wide area. The longer the ray paths are, the wider the sensitivities spread. The phase-delay kernels also exhibit typical banana-doughnut shape (Dahlen *et al.*, 2000; Hung *et al.*, 2000; Zhao *et al.*, 2000) with diminishing amplitude along the ray paths. However, in each of the phase-delay kernels, the doughnut behavior does not extend all the way to either end of the ray path because of the exceptionally large near-field amplitudes in the vicinity of both the source and the receiver. In fact, these phase-delay kernels show that the near-fields have a disproportionally large contribution to the observed travel-time anomalies. The Fréchet kernels for the amplitude reductions are as expected. They

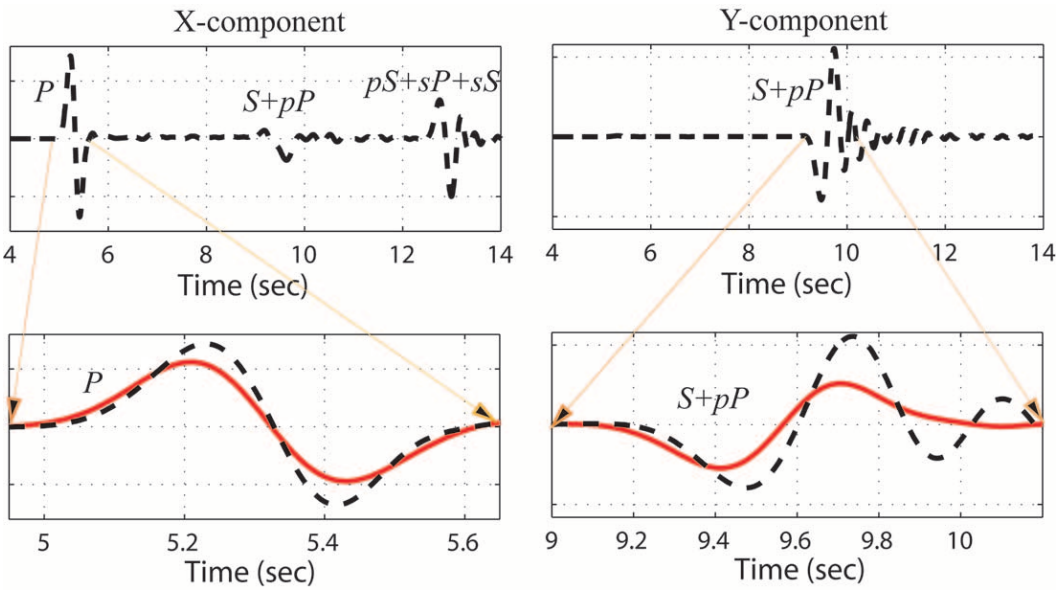

Figure 9. Comparisons of the X- and Y-component seismograms for a double-couple source in the original uniform half-space model and the model with an increase in both *P* and *S* wave speeds around point D as shown in Figures 6 and 7. The black dashed lines are the waveform for the original model and the perturbed waveforms are in red. The model perturbations and the resulting waveform changes are described in the text.

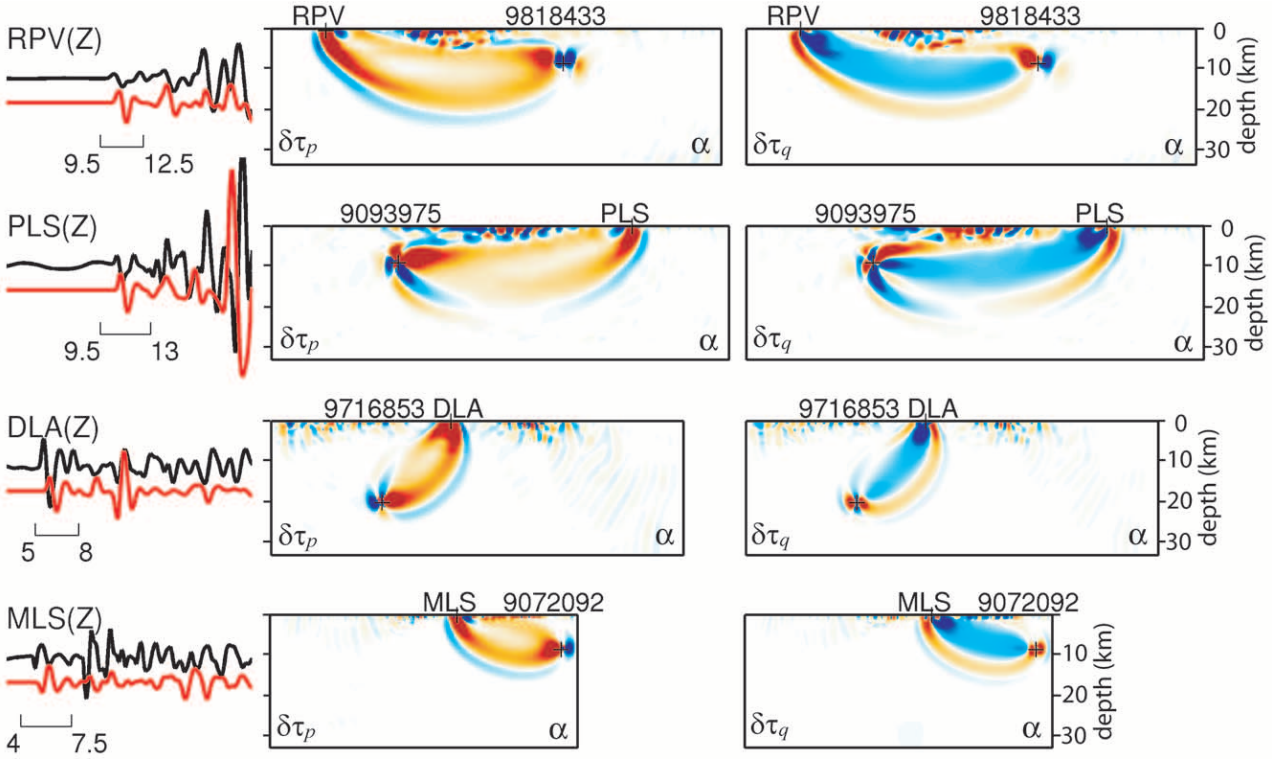

Figure 10. Fréchet kernels of direct *P* waves for *P*-wave speed α along four source-receiver paths shown by the solid lines in Figure 1. Also shown are the recorded (black) and synthetics (red) seismograms. The time windows in which the kernels are computed are also indicated (in sec). All the kernel plots are made in the source-receiver vertical plane. In each box, the two side boundaries are the intersections of the source-receiver vertical plane with the modeling boundary (box in Fig. 1). The crosses indicate the locations of the stations (surface) and the sources (at depth).

are maximum along the ray paths and also have much larger amplitude near the sources and receivers.

In the images of the Fréchet kernels in Figure 10, there are also some regions with highly oscillatory amplitudes. These are possibly the product of three factors. Firstly, the oscillatory patterns near the surface in the kernels for stations RPV and PLS are perhaps caused by the scatterings at the surface or by strong lateral gradients in and around the basin. Secondly, in the kernels for DLA, the oscillatory amplitudes near the surface are physically unexplainable and are probably due to the numerical inaccuracy in the surface and absorbing boundary conditions in the finite-difference simulations. Finally, the spatial Gibbs phenomenon because of the limited bandwidth can also enhance the effects by the previous two factors. In any case, these numerical noises are highly spatially oscillatory and with proper choice of the model cell sizes they are unlikely to have significant effect in tomography inversions.

Figure 11 shows the Fréchet kernels of the direct *S* waves for the *S*-wave speed β on the transverse and radial components along three paths (dashed lines in Figure 1). These kernels are clearly leaner than the *P*-wave ones in Figure 10 because of lower *S*-wave speed hence shorter wavelengths and smaller Fresnel zone widths. These are signals arriving later in the seismograms, and therefore they are much more likely to be the superpositions of multiple arrivals than the first-arriving direct *P* waves. The fact that they are not purely single shortest-path arrivals means that the doughnut phenomenon no longer exists. We can see that the sensitivity is not zero but positive along the ray path for the *SH* wave at CHN, and at RUS the *SH*-wave kernel has a very larger positive amplitude along its ray path, presumably due to strong multipathing effect. This can be confirmed by the synthetic seismogram for RUS in which the *SH* waveform has almost undergone a $\pi/2$ phase shift from the *SH* wave at CHN. These sensitivity kernels for the *S*-wave speed β fill a gap in the studies of local high-resolution shear-wave structures. In the current Harvard and SCEC high-resolution 3D models for Southern California, only the *P*-wave speed is directly obtained from seismic or other observations whereas the *S*-wave structure is always derived from the *P*-wave model using scaling relations. However, the Fréchet kernels for β that we compute here provide a reliable tool to invert for the *S*-wave structure directly from seismic observations and independently from the *P*-wave inversions.

In Figure 12 we display the Fréchet kernels for more complicated phases along four paths (dotted lines in Fig. 1). Because of much more complicated effects such as multipathing and nongeometrical reflections/refractions, the sensitivity patterns no longer suggest coherent ray paths. These arrivals and their Fréchet kernels provide additional sensitivities to the *P*- and *S*- wave speeds, and they are very im-

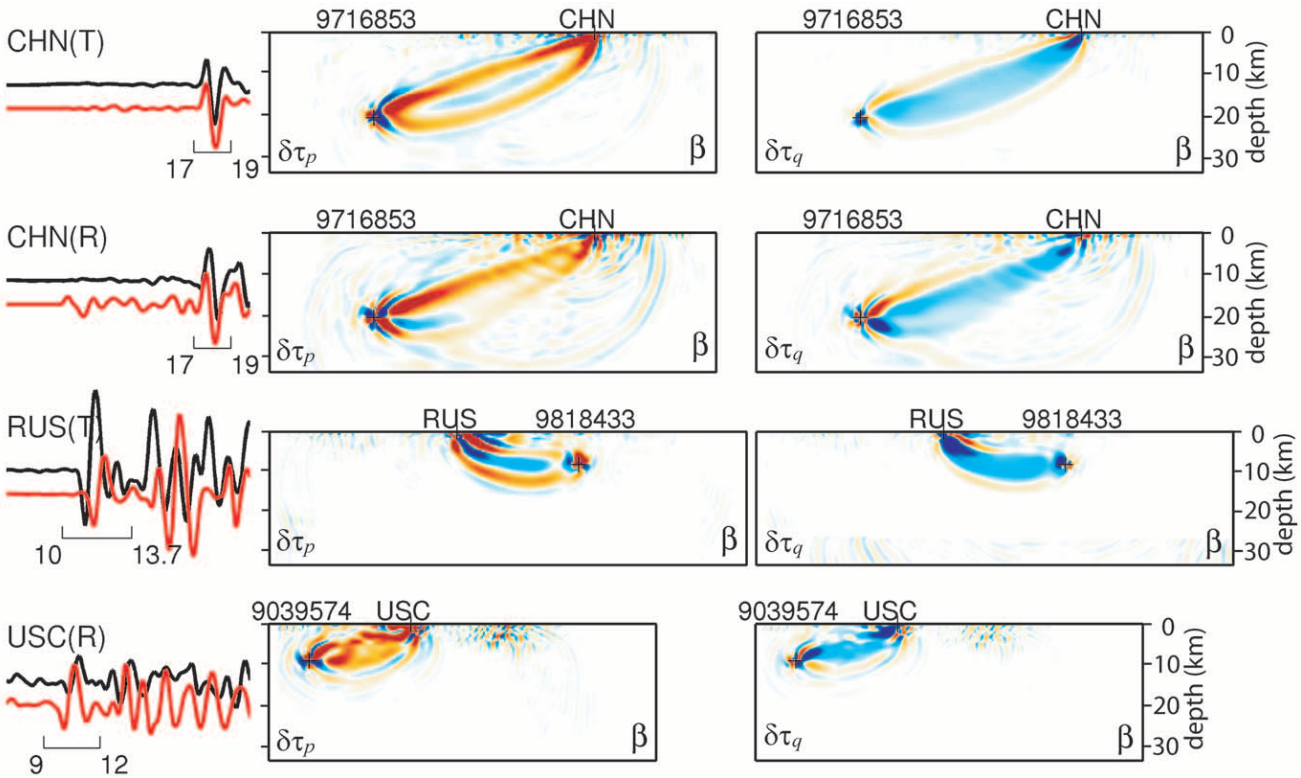

Figure 11. Fréchet kernels of direct *S* waves for *S*-wave speed β along three source-receiver paths shown by the dashed lines in Fig. 1. Also shown are the recorded (black) and synthetics (red) seismograms. The time windows in which the kernels are computed are also indicated (in sec).

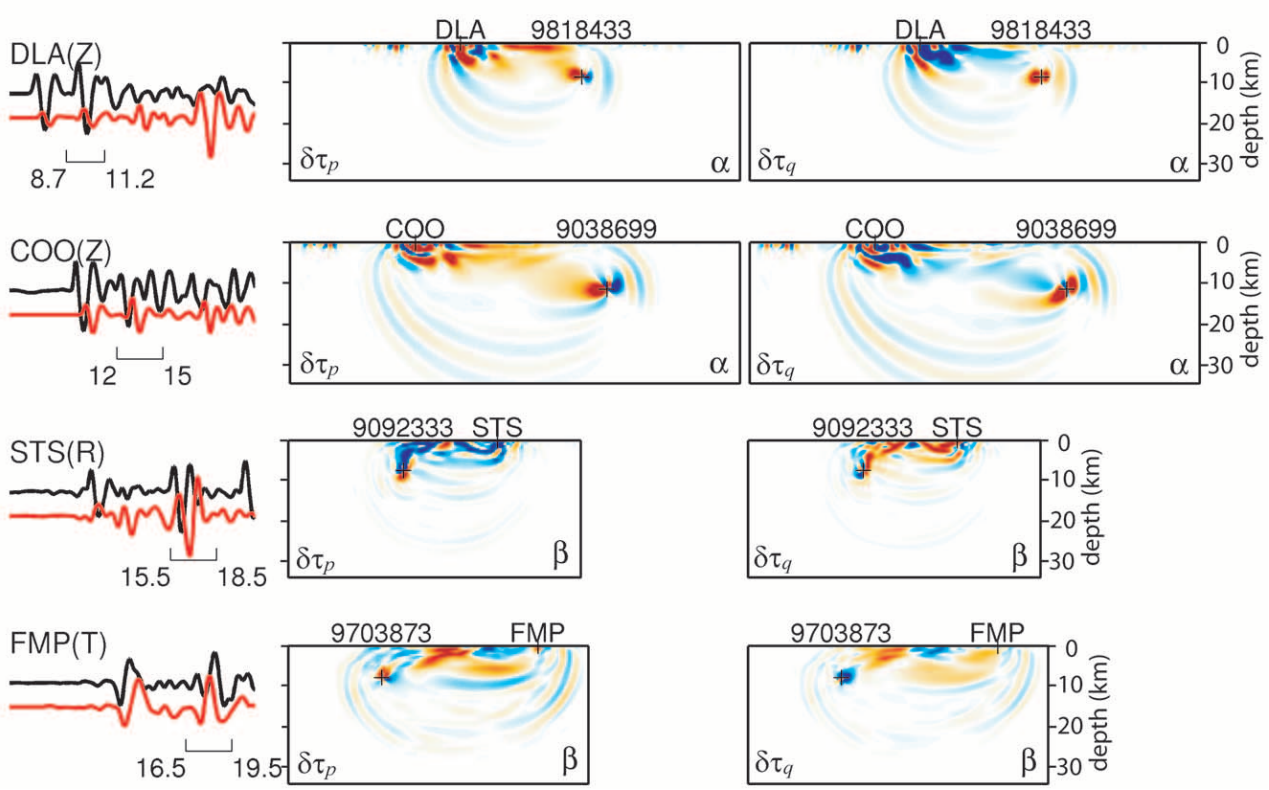

Figure 12. Fréchet kernels of nondirect arrivals for *P*- and *S*-wave speeds along four sourcereceiver paths shown by the dotted lines in Figure 1. Also shown are the recorded (black) and synthetics (red) seismograms. The time windows in which the kernels are computed are also indicated (in sec).

portant in improving the resolution in tomography inversions.

Discussion

We have developed an algorithm to compute accurate 3D Fréchet kernels for delay-time and amplitude anomalies based on complex 3D reference models. The algorithm uses the finite-difference method for the forward wave-propagation modeling. By applying the reciprocity property, the number of finite-difference simulations required can be limited to merely $N_E + 3N_S$, where N_E and N_S are the numbers of events and stations, respectively. Green's tensors for seismic stations from the $3N_S$ simulations can also be used to invert for the centroid-moment tensors and finite-moment tensors of the earthquakes (Chen *et al.*, 2005). This ensures that the N_E simulations for the earthquake-generated wavefields are based on good approximations of the sources. The algorithm can be readily parallelized and is efficient enough for practical tomography studies for the L.A. Basin based on the current regional 3D model.

Numerical results for the travel-time and amplitude kernels demonstrate that for a 3D reference model, the seismic waves interact with the structure in very complicated ways. Even at periods as short as 1.5 sec, the sensitivity kernels display properties much more complex than those expected by ray theory or the strict doughnut phenomenon except in the far fields of the first-arriving *P* wave. The signals on a seismogram after the first arrival are usually difficult to identify and analyze, and the 3D kernels are very useful in visualizing the sources of energy that contribute to the signals and in locating potential problems in the reference model.

The algorithm developed here provides a general and automatic process in establishing the linear relation between the model perturbation and the delay-time and amplitude anomalies measured over any given time windows. The sensitivities of the measurements to any model parameter are obtained without the need to associate the signals to any particular ray paths. For the signals that arrive late in the seismograms and are impossible to model by ray theory or simple layered models, this algorithm is extremely valuable to imaging the subsurface *S*-wave structure because these signals interact much more heavily with the shear-wave structure.

Acknowledgments

We thank Professor Tony Dahlen and an anonymous reviewer for their careful reading of the manuscript and constructive comments. Numerical computations for the Fréchet kernels described in this article were supported in part by the University of Southern California Center for High Performance Computing and Communications (http://www.usc.edu/hpcc). Figure 1 has been produced by the Generic Mapping Tools of Wessel and

Smith (1998). This research is supported by the Southern California Earthquake Center.

References

Aagaard, B. T., J. F. Hall, and T. H. Heaton (2001). Characterization of near-source ground motions with earthquake simulations, *Earthquake Spectra* **17,** no. 2, 177–207.

Aki, K., and P. G. Richards (2002). *Quantitative Seismology*, Second Edition, University Science Books, Sausalito, Calif.

Aoi, S., and H. Fujiwara (1999). 3D finite-difference method using discontinuous grids, *Bull. Seism. Soc. Am.* **89,** 918–930.

Baig, A., F. A. Dahlen, and S.-H. Hung (2003). Traveltimes of waves in random media, *Geophys. J. Int.* **153,** 467–482.

Bao, H., J. Bielak, O. Ghattas, L. F. Kallivokas, D. R. O'Hallaron, J. R. Shewchuk, and J. Xu, (1998). Large-scale simulation of elastic wave propagation in heterogeneous media on parallel computers, *Comput. Meth. Appl. Mech. Eng.* **152,** 85–102.

Chen, P., T. H. Jordan, and L. Zhao (2005). Finite moment tensor of the 3 September 2002 Yorba Linda earthquake, *Bull. Seism. Soc. Am.* **95,** 1170–1180.

Dahlen, F. A., S.-H. Hung, and G. Nolet (2000). Fréchet kernels for finite-frequency travel times, part I: theory, *Geophys. J. Int.* **141,** 157–174.

Davis, P. M., J. L. Rubinstein, K. H. Liu, S. S. Gao, and L. Knopoff (2000). Northridge earthquake damage caused by geologic focusing of seismic waves, *Science* **289,** 1746–1750.

Favier, N., S. Chevrot, and D. Komatitsch (2004). Near-field influence on shear wave splitting and traveltime sensitivity kernels, *Geophys. J. Int.* **156,** 467–482.

Frankel, A., and J. Vidale (1992). A three-dimensional simulation of seismic waves in the Santa Clara valley, California, from the Loma Prieta aftershock, *Bull. Seism. Soc. Am.* **82,** 2045–2074.

Fuis, G. S., T. Ryberg, N. J. Godfrey, D. A. Okaya, and J. M. Murphy (2001). Crustal structure and tectonics from the Los Angeles basin to the Mojave Desert, southern California, *Geology* **29,** 15–18.

Gaherty, J. B., T. H. Jordan, and L. S. Gee (1996). Seismic structure of the upper mantle in a Central Pacific corridor, *J. Geophys. Res.* **101,** 22,291–22,309.

Gee, L. S., and T. H. Jordan (1992). Generalized seismological data functionals, *Geophys. J. Int.* **111,** 363–390.

Godfrey, N. J., V. Langenheim, G. S. Fuis, and D. A. Okaya (2002). Lower crustal deformation beneath the central Transverse Ranges, Southern California: results from the Los Angeles region seismic experiment, *J. Geophys. Res.* **107,** doi 10.1029/2001JB000354.

Gottschammer, E., and K. B. Olsen (2001). Accuracy of the explicit planar free-surface boundary condition implemented in a fourth-order staggered-grid velocity-stress finite-difference scheme, *Bull. Seism. Soc. Am.* **91,** 617–623.

Graves, R. W. (1996). Simulating seismic wave propagation in 3D elastic media using staggered-grid finite differences, *Bull. Seism. Soc. Am.* **86,** no. 4, 1091–1106.

Graves, R., A. Pitarka, and P. Somerville (1998). Ground motion amplification in the Santa Monica area: effects of shallow basin edge structure, *Bull. Seism. Soc. Am.* **88,** 337–356.

Hadley, D., and H. Kanamori (1977). Seismic structure of the Transverse Ranges, California, *Geol. Soc. Am. Bull.* **88,** 1469–1478.

Hauksson, E. (2000). Crustal structure and seismicity distribution adjacent to the Pacific and North America plate boundary in Southern California, *J. Geophys. Res.* **105,** 13,875–13,903.

Hung, S.-H., F. A. Dahlen, and G. Nolet (2000). Fréchet kernels for finite-frequency travel times, part II: examples, *Geophys. J. Int.* **141,** 175–203.

Igel, H. (1999). Wave propagation in three-dimensional spherical sections by the Chebyshev spectral method, *Geophys. J. Int.* **136,** 559–566.

Katzman, R., L. Zhao, and T. H. Jordan (1998). High-resolution, two-dimensional vertical tomography of the central Pacific mantle using *ScS* reverberations and frequency-dependent travel times, *J. Geophys. Res.* **103,** 17,933–17,971.

Kawase, H. (1996). The cause of the damage belt in Kobe: "The basin-edge effect," constructive interference of the direct *S*-wave with the basin-induced diffracted/Rayleigh waves, *Seism. Res. Lett.* **67,** 25–34.

Kohler, M. D. (1997). Three-dimensional velocity structure and resolution of the core-mantle boundary region from whole-mantle inversions of body waves, *Phys. Earth Planet. Int.* **101,** 85–104.

Kohler, M., H. Magistrale, and R. Clayton (2003). Mantle heterogeneities and the SCEC three-dimensional seismic velocity model version 3, *Bull. Seism. Soc. Am.* **93,** 757–774.

Komatitsch, D., Q.-Y. Liu, J. Tromp, M. P. Süss, C. Stidham, and J. H. Shaw (2004). Simulations of ground motion in the Los Angeles Basin based upon the spectral-element method, *Bull. Seism. Soc. Am.* **94,** 187–206.

Komatitsch, D., and J. P. Vilotte (1998). The spectral-element method: an efficient tool to simulate the seismic response of 2D and 3D geological structures, *Bull. Seism. Soc. Am.* **88,** no. 2, 368–392.

Kristek, J., P. Moczo, K. Irikura, T. Iwata, and H. Sekiguchi (1999). The 1995 Kobe mainshock simulated by 3D finite differences, in *The Effects of Surface Geology on Seismic Motion*, K. Irikura, K. Kudo, H. Okada, and T. Sasatani (Editors), Vol. 3, Balkema, Rotterdam, The Netherlands, 1361–1368.

Li, X.-D., and T. Tanimoto (1993). Waveforms of long-period waves in a slightly aspherical earth model, *Geophys. J. Int.* **112,** 92–102.

Li, X.-D., and B. A. Romanowicz (1996). Global mantle shear velocity model developed using nonlinear asymptotic coupling theory, *J. Geophys. Res.* **101,** 22,245–22,272.

Magistrale, H., K. McLaughlin, and S. Day (1996). A geology based 3-D velocity model of the Los Angeles basin sediments, *Bull. Seism. Soc. Am.* **86,** 1161–1166.

Magistrale, H., S. Day, R. W. Clayton, and R. Graves (2000). The SCEC Southern California reference three-dimensional seismic velocity model Version 2, *Bull. Seism. Soc. Am.* **90,** S65–S76.

Marcinkovich, C., and K. B. Olsen (2003). On the implementation of perfectly matched layers in a 3D fourth-order velocity-stress finite-difference scheme, *J. Geophys. Res.* doi 2002JB002235.

Marquering, H., F. A. Dahlen, and G. Nolet (1999). Three-dimensional sensitivity kernels for finite-frequency traveltimes: the banana-doughnut paradox, *Geophys. J. Int.* **137,** 805–815.

McGuire, J. J., L. Zhao, and T. H. Jordan (2001). Teleseismic inversion for the second-degree moments of earthquake space-time distributions, *Geophys. J. Int.* **145,** 661–678.

McLaughlin, K. L., and S. M. Day (1994). 3-D elastic finite-difference seismic wave simulations, *Comput. Phys.* **8,** no. 6, 656–663.

Mégnin, C., and B. Romanowicz (2000). A 3D model of shear velocity in the mantle from the inversion of waveforms of body, surface, and higher mode waveforms, *Geophys. J. Int.* **143,** 709–728.

Olsen, K. B. (1994). Simulation of three-dimensional wave propagation in the Salt Lake Basin, *Ph.D. Thesis*, University of Utah, Salt Lake City, Utah, 157 pp.

Olsen, K. B. (2000). Site amplification in the Los Angeles Basin from 3D modeling of ground motion, *Bull. Seism. Soc. Am.* **90,** S77–S94.

Pitarka, A., K. Irikura, T. Iwata, and H. Sekiguchi (1998). Three-dimensional simulation of the near-fault ground motion for the 1995 Hyogoken Nanbu (Kobe), Japan, earthquake, *Bull. Seism. Soc. Am.* **88,** 428–440.

Süss, M. P., and J. H. Shaw (2003). P-wave seismic velocity structure derived from sonic logs and industry reflection data in the Los Angeles basin, California, *J. Geophys. Res.* **108,** doi 10.1029/2001JB001628, 2003.

Tanimoto, T. (1995). Formalism for traveltime inversion with finite frequency effects, *Geophys. J. Int.* **121,** 103–110.

Tessmer, E., D. Kessler, D. Kosloff, and A. Behle (1992). Multi-domain Chebyshev-Fourier method for the solution of the equations of motion of dynamic elasticity, *J. Comput. Phys.* **100,** 355–363.

Tromp, J., C. Tape, and Q. Liu (2005). Seismic tomography, adjoint methods, time reversal and banana-doughnut kernels, *Geophys. J. Int.* **160,** 195–216.

Wessel, P., and W. H. F. Smith (1998). New, improved version of the Generic Mapping Tools released, *EOS Trans. AGU* **79,** 579.

Zhao, L., and T. H. Jordan (1998). Sensitivity of frequency-dependent traveltimes to laterally heterogeneous, anisotropic Earth structure, *Geophys. J. Int.* **133,** 683–704.

Zhao, L., T. H. Jordan, and C. H. Chapman (2000). Three-dimensional Fréchet differential kernels for seismic delay times, *Geophys. J. Int.* **141,** 558–576.

Zhu, L., and H. Kanamori (2000). Moho depth variation in southern California from teleseismic receiver functions, *J. Geophys. Res.* **105,** 2969–2980.

Zhu, L., and A. Rivera (2002). A note on the dynamic and static displacements from a point source in multi-layered media, *Geophys. J. Int.* **148,** 619–627.

Department of Earth Sciences
University of Southern California
Los Angeles, California
(L.Z., T.H.J., P.C.)

Department of Geological Sciences
San Diego State University
San Diego, California
(K.B.O.)

Manuscript received 19 April 2005.